

1 **Protein and substrate flexibility contribute to enzymatic specificity in human** 2 **and bacterial methionine adenosyltransferases**

3

4

5 Madhuri Gade¹, Li Lynn Tan², Mahakaran Sandhu², Jospheh S. Brock³, Andie Delaney², Alejandro
6 Villar-Briones¹, Colin J. Jackson^{*2,4,5}, Paola Laurino^{*1}

7

8 ¹Okinawa Institute of Science and Technology Graduate University, 1919-1 Tancha, Onna-son,
9 Kunigami, Okinawa 904-0495, Japan

10 ² Research School of Chemistry, Australian National University, Canberra, 2601, Australia

11 ³ Research School of Biology, Australian National University, Canberra, 2601, Australia

12 ⁴ Australian Research Council Centre of Excellence for Innovations in Peptide and Protein Science,
13 Research School of Chemistry, Australian National University, Canberra, 2601, ACT, Australia

14 ⁵ Australian Research Council Centre of Excellence in Synthetic Biology, Research School of
15 Chemistry, Australian National University, Canberra, 2601, ACT, Australia

16

17

18 **Abstract**

19 Protein conformational change can facilitate the binding of non-cognate substrates and underlie
20 promiscuous activities. However, the contribution of substrate conformational dynamics to this
21 process is comparatively poorly understood. Here we analyse human (hMAT2A) and *Escherichia*
22 *coli* (eMAT) methionine adenosyltransferases that have identical active sites but different substrate
23 specificity. In the promiscuous hMAT2A, non-cognate substrates bind in a stable conformation to
24 allow catalysis. In contrast, non-cognate substrates rarely sample stable productive binding modes
25 in eMAT owing to increased mobility of an active site loop. Different cellular concentrations of
26 substrate likely drove the evolutionary divergence of substrate specificity in these orthologs. The
27 observation of catalytic promiscuity in hMAT2A led to the detection of a new human metabolite,
28 methyl thioguanosine, that is produced at elevated level in a cancer cell line. This work establishes
29 that identical active sites can result in different substrate specificity owing to the combined effects
30 of both enzyme and substrate dynamics.

31

32

1 **Introduction**

2 Enzymes can exhibit promiscuous activities with non-cognate ligands that are not involved in the
3 main physiological function of the enzyme¹. These promiscuous activities are often vestigial traits
4 of a distant ancestor² or have originated by chance through evolution³⁻⁶. The importance of
5 promiscuous enzymatic activities is becoming increasingly evident, as they have been shown to
6 contribute to evolvability⁷, stress responses⁸ and, potentially, susceptibility to disease⁸⁻¹⁰. Protein
7 conformational sampling has been shown to play a role in substrate promiscuity¹¹⁻¹⁴, as
8 conformational change can allow enzyme to occasionally sample alternative conformations with
9 different charge preorganization, allowing different transition states to be stabilized¹⁵. While the
10 role of protein structural dynamics in this process has been described, the role of substrate
11 conformational sampling is comparatively poorly understood. It has recently been reported that
12 large active sites can accommodate multiple different productive substrate conformations without
13 changing the conformation of the catalytic pocket^{16,17}, and that in some cases new Michaelis
14 complexes can be recognized¹⁸.

15
16 The methionine adenosyltransferases (MATs), are found in all kingdoms of life and the product of
17 their reaction, S-adenosyl-L-methionine (SAM), is a necessary metabolite in several essential
18 cellular processes¹⁹⁻²¹. Because of the physiological importance of SAM, dysfunction in the
19 production of SAM by MATs can lead to disease^{22,23}. Mechanistically, the enzyme-catalyzed
20 formation of S-adenosyl-L-methionine (SAM) from adenosine triphosphate (ATP) and methionine
21 occurs in two steps²⁴: first, SAM is formed by S_N2 attack by the sulfur of methionine at the C5
22 carbon of ATP, followed by hydrolysis of triphosphate (PPPi) into pyrophosphate (PPi) and
23 orthophosphate (Pi)²⁵ (Figure 1a). This second step is believed to provide the energy required for
24 the conformational rearrangement of the enzyme necessary for product release²⁶. Two Mg²⁺ ions
25 are involved in coordination of the triphosphate moiety of ATP and K⁺ is known to enhance the
26 reaction rate by allowing the active site to adopt the optimal conformation^{20,27,28}.

27
28 MATs are an excellent model system for the study of substrate promiscuity because the chemical
29 reactivity of the cognate physiological nucleotide substrate, ATP, is independent from the
30 nucleobase²⁹. Moreover, SAM is not an intrinsically better methyl donor than the potential
31 products from promiscuous reactions with non-cognate NTPs (S-guanosyl-L-methionine (SGM),

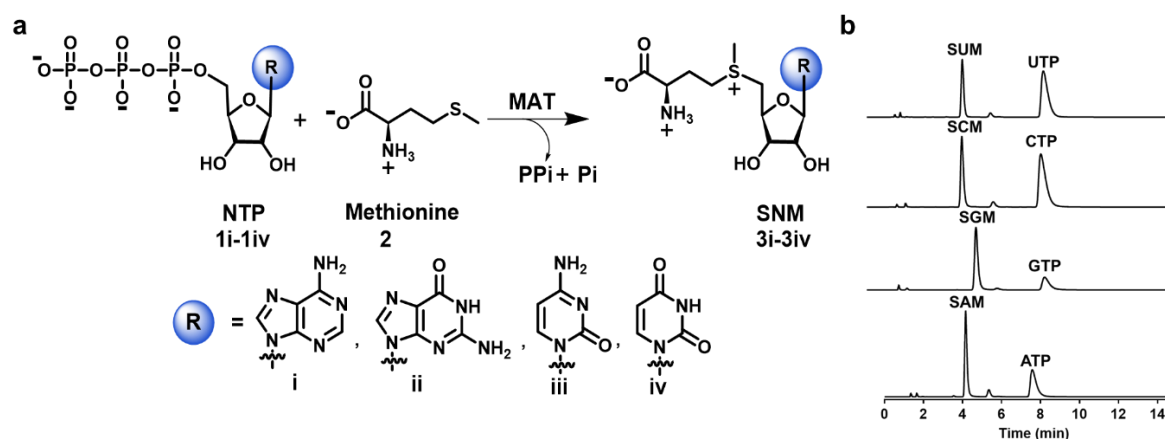
1 S-cytidyl-L-methionine (SCM), or S-uridyl-L-methionine (SUM)), since the nucleotide base does
2 not influence the sulfonium reactivity. While *E. coli* MAT has been reported to display specificity
3 for ATP *in vitro*²⁷, the promiscuity of human MAT for GTP, CTP and UTP has not been
4 systematically explored *in vitro* or *in vivo*.

5
6 In this work, we have performed a systematic study of the substrate promiscuities of human
7 (hMAT2A) and *E. coli* (eMAT) MATs. We show that hMAT2A, unlike eMAT, exhibits substrate
8 promiscuity towards other non-cognate NTPs. Structural analysis reveals that eMAT specificity is
9 a consequence of a lack of structural constraint on the non-cognate substrates, which results from
10 increased active site loop dynamics *vs.* hMAT2A. The increased conformational freedom of the
11 non-cognate substrates results in them sampling catalytically non-productive states at higher
12 frequency than the native substrate, ATP, providing a molecular explanation for the observed
13 enzyme kinetics. We demonstrate that the substrate promiscuity of hMAT2A is relevant *in vivo*
14 and this knowledge allowed us to identify a new metabolite, methyl thioguanosine, a breakdown
15 product of SGM, that is produced in a human liver cancer cell line but was not produced at
16 detectable levels in a normal liver cell line.

17
18
19
20
21
22
23

1 Results

2 **The catalytic promiscuity of MATs.** For the kinetic analysis of eMAT and hMAT2A, we
3 developed a sensitive and specific assay based on ultra-performance liquid chromatography
4 (UPLC) (see Methods). This allowed us to analyze the generation of different S-(nucleoside)-L-
5 methionine (SNM) analogs with confirmation of the products *via* mass spectrometry (Figure 1b;
6 Appendix). From these data, kinetic parameters were derived (Table 1; Supplementary Figure 1).
7 hMAT2A efficiently catalyzed the formation of SGM, SCM and SUM, in addition to the cognate
8 product, SAM. No spontaneous product formation was observed without MAT (Supplementary
9 Figure 2a). The activity of hMAT2A with the four different nucleotides varied over a relatively
10 narrow range (k_{cat}/K_M values of non-cognate substrates within 42-93% of ATP; Table 1. The
11 k_{cat}/K_M of eMAT with ATP was comparable to that of hMAT2A (Table 1), albeit with lower k_{cat}
12 and K_M values. However, the activity of eMAT for other nucleotides differed: the k_{cat}/K_M of eMAT
13 was 61-fold, 8.5-fold and 139-fold lower for GTP, CTP and UTP respectively., than for ATP
14 (Table 1; Supplementary Figure 1). Thus, while hMAT2A is catalytically promiscuous with
15 various NTPs, eMAT is comparatively specific (Supplementary Figure 2b).



16
17 **Figure 1. SNM biochemical synthesis, identification of SNM analogs by UPLC.** a) Synthesis
18 of S-nucleoside-L-methionine (SNM) analogs S-adenosyl-L-methionine (3i, SAM), S-guanosyl-L-
19 methionine (3ii, SGM), S-cytidyl-L-methionine (3iii, SCM), S-uridyl-L-methionine (3iv, SUM)
20 from different nucleotides (ATP, GTP, CTP, UTP) and methionine. b) UPLC chromatograms of the
21 reaction of NTPs (5 mM) and methionine (10 mM) in presence of hMAT2A (20 μ M) (1h, 37 $^{\circ}$ C,
22 details are in the Methods section). Noted are the peaks corresponding to SAM ($t_R = 4.1$ min),
23 SCM ($t_R = 4.6$ min), SUM ($t_R = 4.6$ min), SGM ($t_R = 5.3$ min), ATP ($t_R = 7.5$ min), GTP ($t_R = 7.8$ min),
24 CTP ($t_R = 8.3$ min) and UTP ($t_R = 8.5$ min).

25
26
27
28

1 **Table 1. Kinetic parameters* for the SNM analog formation by hMAT2A and eMAT**

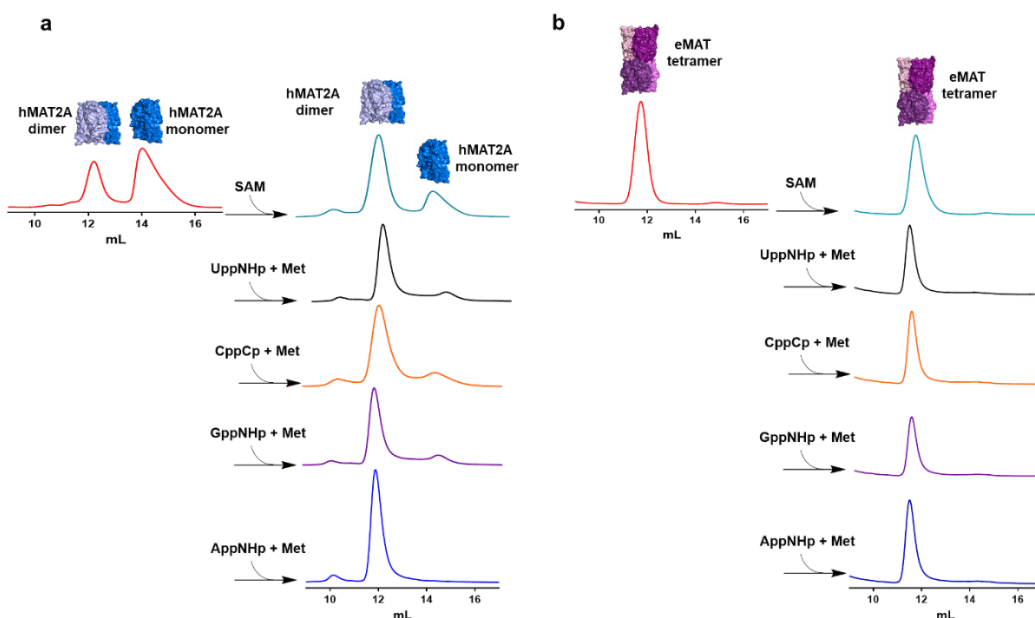
Enzyme: Substrate	k_{cat} (s^{-1})	K_M (mM)	k_{cat}/K_M ($M^{-1}s^{-1}$)
hMAT2A: ATP	764 ± 61	0.27 ± 0.07	2.8×10^6
hMAT2A: GTP	3270 ± 600	1.26 ± 0.40	2.6×10^6
hMAT2A: CTP	100 ± 4.8	0.08 ± 0.02	1.3×10^6
hMAT2A: UTP	1180 ± 140	0.97 ± 0.2	1.2×10^6
eMAT: ATP	66 ± 4	0.06 ± 0.02	1.1×10^6
eMAT: GTP	18 ± 2	0.97 ± 0.30	1.8×10^4
eMAT: CTP	168 ± 12	1.3 ± 0.25	1.3×10^5
eMAT: UTP	23 ± 3	2.90 ± 0.7	7.9×10^3

2
3 * Kinetic parameters for the SNM analog formation by hMAT2A, eMAT using a concentration of
4 ATP, GTP, CTP and UTP in the range of 0.025 to 5 mM and a fixed saturating concentration of
5 methionine (10 mM) in the presence of HEPES (100 mM), KCl (50 mM), $MgCl_2$ (10 mM), pH 8 at
6 37 °C. [hMAT2A] was 0.5 μM and [eMAT] concentrations were 0.5 μM for ATP, 5 μM for GTP,
7 CTP and 10 μM for UTP. SNM production was analyzed by UPLC and data fitted to the Michaelis-
8 Menten equation using GraphPad Prism (Supplementary Figure 1).
9

10 **The molecular basis for MAT specificity.** We investigated three alternative explanations that
11 could explain the difference in catalytic specificity between eMAT and hMAT2A: (i) different
12 oligomeric states; (ii) residue differences in the substrate binding pockets; (iii) different
13 conformational sampling/protein dynamics, caused by sequence differences in regions remote
14 from the active site.

15
16 (i) *Oligomeric state.* The active sites of both enzymes are located at the dimer interface^{30,31}.
17 Accordingly, we investigated whether differences between the native oligomeric states of either
18 eMAT or hMAT2A underlie their different substrate specificity. We used the NTP analogues
19 adenosine-5'-[(β , γ)-imido]triphosphate (AppNHp), guanosine-5'-[(β , γ)-imido]triphosphate
20 (GppNHp), cytidine-5'-[(β , γ)-methylene] triphosphate (CppCp), and uridine-5'-[(β , γ)-
21 imido]triphosphate (UppNHp)], since the MATs can catalyze the transferase step of the reaction
22 to yield SNM analogues, but triphosphate hydrolysis cannot proceed and the product-bound state
23 is thus trapped in the catalytic binding pocket (at least for the timescale of these experiments)³².
24

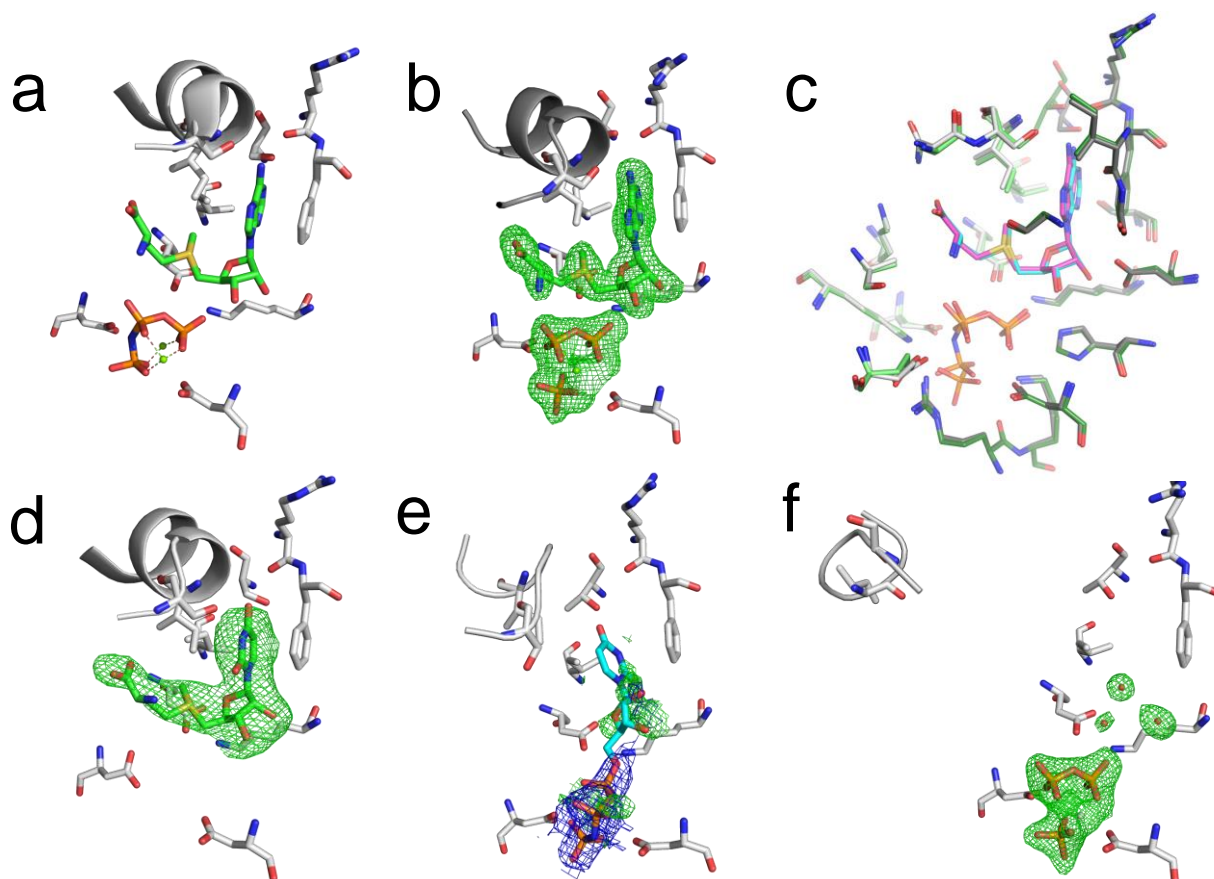
1 We confirmed using size exclusion chromatography that apo-hMAT2A exists in equilibrium
2 between monomeric (63%) and dimeric (37%) states (Figure 2a), whereas apo-eMAT is tetrameric
3 (Figure 2b). The oligomeric equilibrium of hMAT2A shifts almost entirely towards the dimeric
4 state upon incubation with the NTP analogues and methionine (Figure 2a). If any of a
5 nonhydrolyzable NTP, methionine, triphosphate or SAM were added alone (i.e., if the ternary
6 Michaelis complex is unable to form), no change in the oligomeric state was observed
7 (Supplementary Figure 3a). This result suggests that formation of the ternary Michaelis complex
8 (enzyme: NTP: Met) drives dimer formation in the case of hMAT2A. In the case of eMAT, no
9 change in oligomeric state was observed (Figure 2b and Supplementary Figure 3b). Because there
10 were no observed differences between the cognate and non-cognate analogs with either enzyme,
11 it can be concluded that the differences in substrate specificity are independent of the oligomeric
12 state of the enzymes.



13
14 **Figure 2. Analysis of oligomeric state of hMAT2A and eMAT by size exclusion**
15 **chromatography. a)** hMAT2A (20 μ M) is incubated with nonhydrolyzable NTPs (1 mM)
16 adenosine-5'-[(β , γ)-imido]triphosphate (AppNHp), guanosine-5'-[(β , γ)-imido]triphosphate
17 (GppNHp), cytidine-5'-[(β , γ)-methylene] triphosphate (CppCp), uridine-5'-[(β , γ)-
18 imido]triphosphate (UppNHp)] together with methionine (Met, 10 mM) using reaction buffer (100
19 mM HEPES, 10 mM KCl, 10 mM MgCl₂, pH 8, 37°C for 1 hr). hMAT2A is in an equilibrium of a
20 monomer and dimer. When incubated with both substrates convert completely in dimeric state.
21 No change in oligomeric state when incubated with both substrates and SAM was observed. **b)** eMAT (20 μ M) is incubated using the
22 same condition as used for hMAT2A. eMAT is in a tetrameric state and no change in oligomeric
23 state after incubating with both substrates and SAM was observed. Size exclusion
24 chromatography was performed using GE Healthcare Life Sciences using Superdex 200 Increase
25 10/300 GL column.

1
2 (ii) *The substrate binding site.* To investigate the structural basis for substrate promiscuity, we then
3 solved structures of eMAT and hMAT2A in complex with various substrates and substrate
4 analogues (Supplementary Table 1). The structure of hMAT2A in complex with SAM and
5 imidotriphosphate (PPNP) has previously been reported³¹ (Figure 3a). Here we solved a crystal
6 structure of eMAT in the presence of ATP and methionine, which enabled us to capture the SAM
7 product-bound state of eMAT at a resolution of 1.95 Å (Figure 3b). This allowed us to align the
8 eMAT:SAM structure to the previously published hMAT2A:SAM structure (Figure 3c). The
9 active site structures of eMAT and hMAT2A were essentially identical; the only difference was
10 that the eMAT structure has pyrophosphate (PPi) and orthophosphate (Pi) bound in the lower part
11 of the active site, whereas the hMAT2A structure has PPNP bound in the same position (the
12 substrate in the hMAT2A protein crystal being the analogue AppNHp, rather than ATP).
13 Regarding the nucleoside binding region, we observe stabilizing interactions between the enzyme
14 and adenine ring that include a π -stacking interaction (3.5 Å) with Phe230/250 (eMAT/hMAT2A
15 numbering) and hydrogen bonds between the amine group of the adenine ring and the carbonyl
16 oxygen of Arg229/249 and the N1 adenine nitrogen with the side chain of Thr227/Ser227. Closure
17 of the active site loop brings Ile102/117 close to the adenine ring, forming van der Waals contacts.
18
19 The alignment of the residues within the active site is strikingly similar, both in terms of identity
20 (20/21) and structure (r.m.s.d. 0.5 Å). Indeed, every amino acid side chain adopts the same rotamer
21 and the product is bound in an identical conformation. The only difference between the two
22 structures is a conserved substitution at position 227/247 (Thr in eMAT vs. Ser in hMAT2A;
23 Supplementary Figure 4). To investigate the effect of this substitution, we made Ser247Thr and
24 Thr227Ser mutants in hMAT2A and eMAT, respectively. Neither mutation resulted in any
25 significant change in substrate specificity in either enzyme (Supplementary Figures 5). Thus, the
26 amino acid composition and structures of the substrate binding sites of the two enzymes do not
27 explain the observed differences in their substrate specificity.

28



1
2 **Figure 3. The substrate binding sites of eMAT and hMAT2A with bound ligands.** Omit electron
3 density (mF_o-DF_c) is shown in green mesh (3.0σ), $2mF_o-DF_c$ density is shown as blue mesh (1.5σ).
4 (a) The published structure of hMAT2A bound to the products SAM and PPNP (PDB ID 5A1I). (b)
5 eMAT with bound products SAM, PPI and Pi obtained via cocrystallization with ATP and methionine.
6 (c) A superimposition of the substrate binding sites of eMAT (green, cyan SAM, PPI and Pi) and
7 hMAT2A (grey, magenta SAM, PPNP). The binding site is comprised of two chains within a
8 homodimer; these are distinguished by light/dark colouring. (d) hMAT2A in complex with SUM after
9 cocrystallization with UppNHp. (e) eMAT cocrystallized with UppNHp (2.1 \AA); the PPNP group is
10 included in the model and shown with $2mF_o-DF_c$, ambiguous omit density potentially corresponding to
11 disordered substrate/product is shown. A poorly fitting model of UppNHp is shown in stick
12 representation (cyan). (f) eMAT bound to the products PPI and Pi (1.88 \AA), with the active site loop
13 captured in the “wide-open” conformation obtained *via* cocrystallization with CTP and methionine.
14

15 To better understand the structural basis for catalytic promiscuity in hMAT2A, we co-crystallized
16 with the non-cognate substrate UTP analog, UppNHP and solved the structure to 2.5 \AA resolution.
17 Imido-NTP analogs have been used as partial inhibitors of MAT because, while they are still

1 substrates for the first methionine transfer step and form the various SNM products, the imido-
2 linkage between the β - γ phosphate units prevents hydrolysis of triphosphate moiety³².
3 Triphosphate hydrolysis is thought to provide energy for active site loop (residues 113-131 in
4 hMAT2A, 98-108 in eMAT) opening and product release^{28,31}. The structure revealed the product
5 SUM bound at high occupancy within the active site (Figure 3d) and was mostly identical to the
6 structure of hMAT2A in complex with SAM. One difference that is not relevant to the
7 nucleoside/SNM binding region is the observation that the PPNP group is completely absent in the
8 structure. The active site loop was fully closed and interacted with SUM in the same manner as
9 with SAM, and the π -stacking interaction with Phe250 was present. The main difference was that
10 the hydrogen bond between the amine group of the adenine and the carbonyl oxygen of Arg249 is
11 not present, although a hydrogen bond between the hydroxyl group of the uridine ring and Ser247
12 is observed. The close similarity between the hMAT2A:SAM and hMAT2A:SUM complexes is
13 consistent with the similar rates of the UTP and ATP turnover observed in the enzyme kinetics
14 (Table 1), suggesting both substrates are stable in catalytically competed configurations.

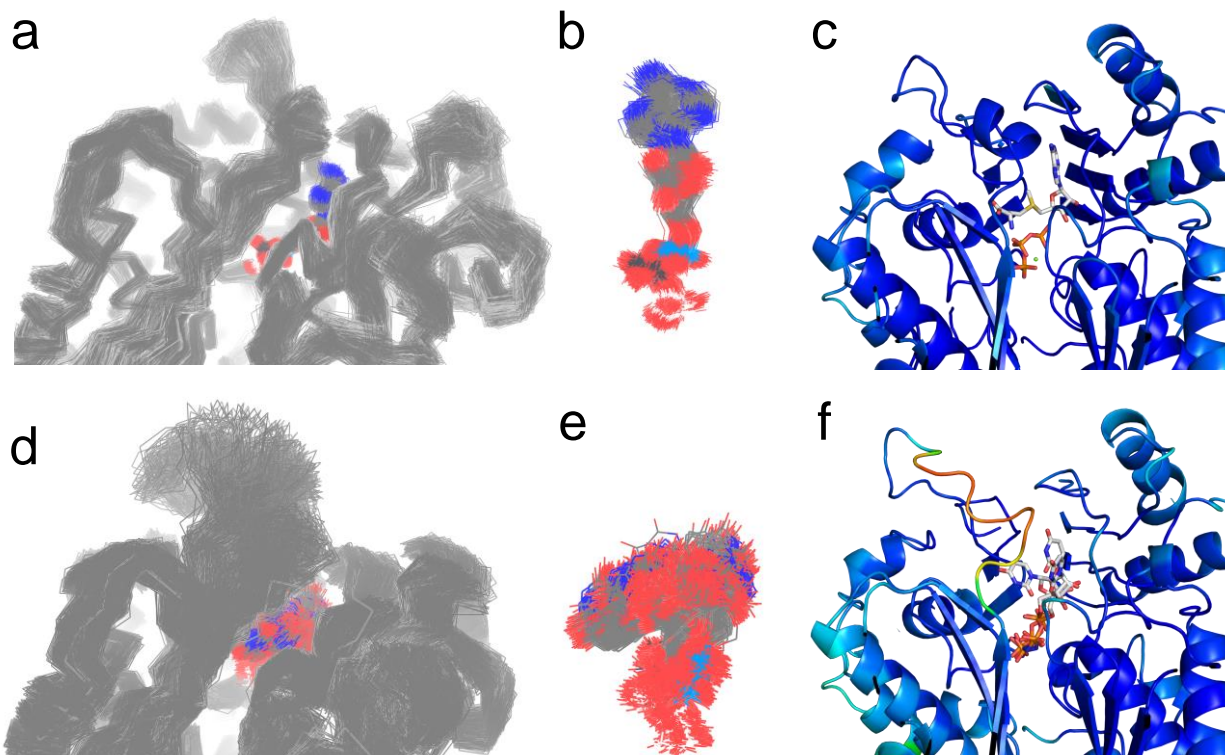
15
16 In contrast to the eMAT:ATP, hMAT2A:ATP and hMAT2A:UppNHp structures, when eMAT
17 was co-crystallized with non-cognate NTPs (CTP/UTP/GTP) we did not observe electron density
18 for any SNM product. Within the active site of the 1.89 Å resolution CTP co-crystal, clear
19 difference density for the PPI and Pi products was observed (Figure 3), although there is
20 unambiguously no electron density for the SCM product. Ordered water molecules were
21 observable, suggesting the SCM had fully diffused from the active site. The active site loop, which
22 was stable and closed in the SAM structure, was instead observed in a “wide-open” conformation,
23 which we believe is the first time this fully open conformation has been fully modelled. For the
24 co-crystals of eMAT with UTP (2.25 Å) and GTP (2.39 Å), which crystallized in a different space
25 group to CTP (Supplementary Table 1), we again observe PPI and Pi in good electron density
26 (Supplementary Figure 6). Like the CTP co-crystal, we do not observe density for the products of
27 the methionine transferase reaction. In these crystals the density in this region appears to
28 correspond to a phosphate molecule, which has presumably re-bonded to the protein after
29 hydrolysis. In these UTP/GTP co-crystals, the active site loop is neither closed, as in the
30 eMAT:SAM structure, nor wide-open, as in the eMAT:CTP co-crystal. Instead, it adopts a
31 disordered intermediate conformation. These results suggest that the non-adenine containing SNM

1 products are less stable within the active site of eMAT than SAM, consistent with eMAT being
2 selective for ATP.

3
4 Finally, the co-crystals of eMAT with UppNHp (2.24 Å) and GppNHp (2.50 Å) displayed clear
5 electron density for the PPNP group and weaker electron density in the nucleoside binding region.
6 This density is not consistent with re-bound phosphate, as observed in the GTP/UTP co-crystals
7 (Supplementary Figure 6), both because of the non-tetrahedral shape of the density and the
8 observation that there is no way that free phosphate could be present in these crystals, since the
9 substrate analog cannot undergo hydrolysis between the β - γ phosphodiester bond, as for the NTPs.
10 The density also extended continuously from the PPNP moiety (Supplementary Figure 6). Finally,
11 the active site loop was in a partially open, disordered, conformation. The poor electron density
12 for the nucleoside groups in these structures could be due to either (or a combination of) disordered
13 binding of the nucleoside moiety of the substrate or diffusion/disorder of the SUM/SGM product.
14 Even if the weaker density is fully due to substrate turnover and diffusion of SUM/SGM, this
15 behavior is very different to the eMAT:ATP and hMAT2A:UppNHp structures, in which the
16 product was clearly stable within the active site. Thus, in contrast to hMAT2A, which interacts in
17 an essentially identical manner with ATP and the non-cognate substrates, eMAT appears to be
18 selective for adenine-containing substrates, because the adenine containing nucleoside moiety is
19 more stable within the active site, which is again consistent with the enzyme kinetics (Table 1).

20
21 *(iii) Differences in protein and ligand dynamics.* The crystallographic analysis of the
22 UppNHp/GppNHp:eMAT complexes suggested the poor density could be due, at least in part, to
23 a disordered substrate binding mode. To examine this possibility in more detail, we performed
24 molecular dynamics (MD) simulations of eMAT in complex with both ATP and UTP to investigate
25 whether there were significant differences between the enzyme:substrate interactions that could
26 explain the specificity for ATP. In order not to bias these simulations, both simulations began with
27 a starting model in which the loop was fully closed over the active site, i.e., the eMAT:UTP bound
28 structure was modelled on the stable SUM bound structure observed in hMAT2A to position of
29 the uridine moiety (Figure 4).

30



1
2 **Figure 4. Conformational dynamics of eMAT:ATP and eMAT:UTP complexes.** (a) Overlay of 250
3 states (1/ns) from a molecular dynamics trajectory of the eMAT:ATP complex. (b) Isolated view of the
4 structural dynamics of ATP over 250 ns (250 states). (c) Structure of eMAT in complex with the
5 products of SAM, pyrophosphate and phosphate (shown as sticks). The protein is shown in cartoon
6 representation, coloured by B-factor). (d) Overlay of 250 states (250 states) from a molecular dynamics
7 trajectory of the eMAT:ATP complex, showing increased mobility of the active site loop. (e) Isolated
8 view of the structural dynamics of UTP over 250 ns (250 states), showing sampling of multiple
9 configurations. (f) Structure of eMAT cocrystallized with UppNHp (shown in multiple plausible states
10 as sticks). The protein is shown in cartoon representation, coloured by B-factor, highlighting the
11 increased mobility of the active site loop.

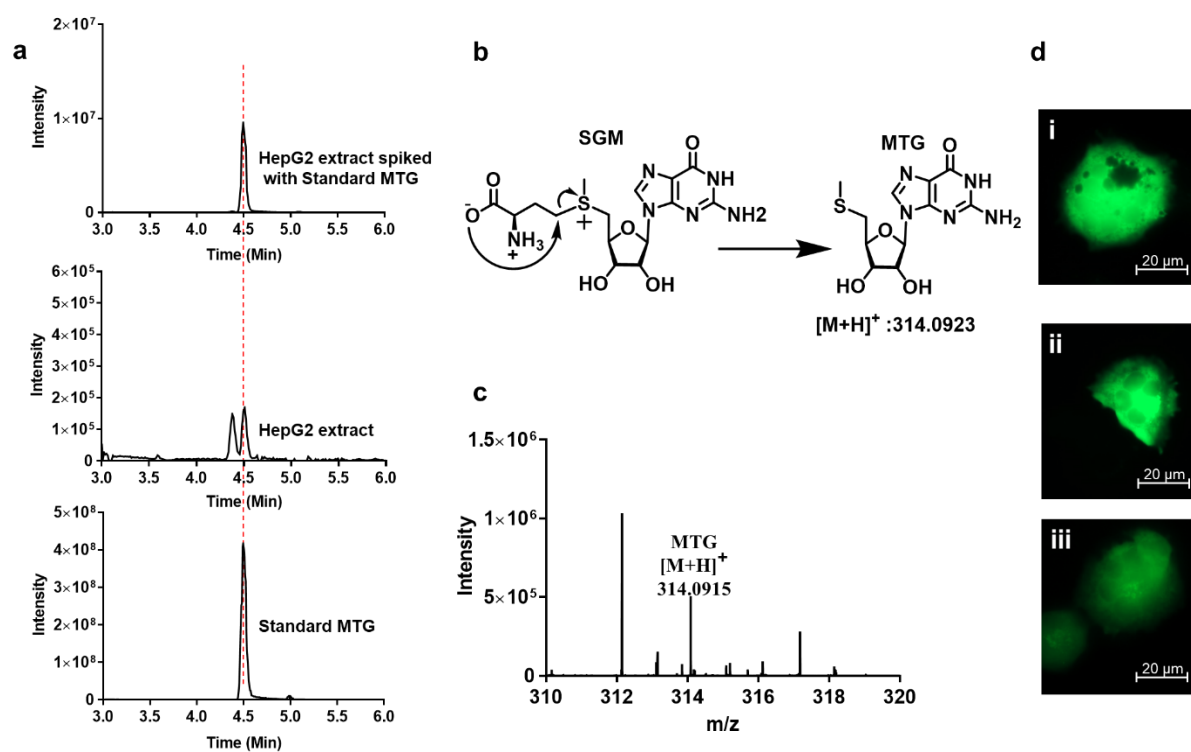
12
13 Triplicate 250 ns simulations of the eMAT:ATP complex showed that the triphosphate, sugar, and
14 purine moieties were stable throughout the simulation, with the purine ring being stabilized by the
15 well-characterized interactions with Phe230, Arg229 and Thr227 (Figure 3 and 4; Supplementary
16 Figure 7). The mobile active site loop was fully stable in the closed state and Ile102' maintained
17 contact with the substrate for most of the simulations. In 1/3 replicates the active site loop opened
18 after ~60 ns and was stable in the open conformation (Supplementary Figure 8); the substrate
19 retained the stable productive binding pose. In contrast, the simulations with UTP took much

1 longer to equilibrate, with the enzyme maintaining a productive “closed” conformation for ~50 ns
2 in all 3 simulations, resulting in significantly higher RMSF for this loop region in the UTP vs. ATP
3 simulations (Supplementary Figure 9). After ~50 ns sequence of events then occurred over the
4 following ~150 ns similarly in all the simulations: first, the pyrimidine ring rotates out of the
5 pocket formed by Ile102’, Phe230, Arg229 and Thr227, followed by opening of the active site
6 pocket to adopt a disordered “wide-open” conformation (with random fluctuations back to the
7 closed state), resulting in the substrate adopting a variety of non-productive binding modes within
8 the active site that essentially block binding and nucleophilic attack from methionine
9 (Supplementary Figures 10 & 11). Thus, the structural dynamics of the active site loop, which are
10 enhanced in the case of UTP owing to fewer stabilizing reactions than with the larger purine group
11 in ATP, result in an opening of the active site that provides conformational freedom for the non-
12 cognate NTP to adopt non-productive binding modes. These observations are consistent with the
13 disorder in the active site loop and the poor electron density for the nucleoside moieties in the
14 substrates/products from co-crystallization with CTP/UTP/GTP/UppNHp/GppNHp (Figure 3), as
15 well as the observed substrate specificity of eMAT (Table 1). It is important to note that these
16 results show that productive binding of non-cognate NTPs can occur (consistent with slow
17 turnover), but that they are less stable/frequent in eMAT than in hMAT2A.

18
19 **The promiscuity of hMAT2A is relevant *in vivo*.** Having established that hMAT2A is
20 promiscuous, and eMAT is specific we compared the reported the physiological concentrations of
21 these NTPs in human³³ and *E. coli*³⁴ cells (Supplementary Table 2): in human cells, the
22 concentration of ATP is ~2.5 mM and the other NTPs (GTP 0.2 mM, CTP 0.08 mM and UTP 0.2
23 mM) are almost 10-fold lower, whereas in *E. coli* the NTPs are all present at similar concentrations.

24
25 We then investigated whether the promiscuous products of hMAT2A could be detected *in vivo*.
26 We performed metabolite analysis of SNM abundance using liquid chromatography-mass
27 spectrometry (LC-MS) of extracts from the normal human liver cell line THLE-2 and the
28 hepatocarcinoma cell (HCC) line HepG2, in which hMAT2A is known to be upregulated³⁵⁻³⁷.
29 Notably, we observed the breakdown product of SGM, methionine thioguanosine (MTG), in the
30 HepG2 cell line (Figure 5a) and not in a THLE-2 (Supplementary Figure 12). As a control, we
31 could detect SAM and MTA in both the samples (Appendix). To the best of our knowledge, there

1 is no other way to form MTG other than from SGM (Figure 5b). The presence of MTG was
2 confirmed by mass spectrometry analysis (Figure 5c). It is unclear whether MTG formed during
3 the extraction procedure or is generated endogenously in the cells. However, SNM analogs were
4 found to have comparable stability in aqueous buffer over the same period. (Supplementary Figure
5 13), suggesting SGM is not significantly less stable and more prone to degradation. Even though
6 the K_M of hMAT2A with CTP (0.08 mM) is lower than for ATP (0.27 mM) we did not detect SCM
7 or MTC analogs in any of the cell lines within the sensitivity range of the experiment; most likely
8 due to the lower CTP concentration within the cells (0.083 in normal cells and 0.4 mM in cancer
9 cells).



10
11 **Figure 5. LC-MS analysis of metabolite and effect of SGM, SAM on HepG2.** a) Extracted
12 chromatograms of the standard MTG, HepG2 cell extract, cell extract samples spiked with the
13 standard MTG. Experiment was performed in biological triplicate. b) Schematic representation of
14 degradation of SGM in to MTG after attack of carboxylate on the γ carbon atom of the methionine. c)
15 Mass spectrum of HepG2 extract showing the mass of MTG $[M+H]^+$ 314.0915. Data was collected
16 using a Q-Exactive HF mass spectrometer coupled with Waters UPLC ACQUITY M-Class liquid
17 chromatography system. An analytical column (ACQUITY UPLC HSS T3 1.8 μ m, 1.0 x 150 mm) was
18 used for sample chromatographic separation. d) Fluorescence microscopy images showing no
19 morphological effect of SGM and SAM on HepG2 cells. HepG2 cells electroporated with (i) pmaxGFP

1 plasmid and with (ii) 1 mM SAM, (iii) 1 mM SGM. Imaging is done using Celldiscover 7 microscope
2 with 20X resolution with 2x magnification changer.

3
4 After the inferred identification of SGM in liver cancer cells, we investigated whether SGM
5 resulted in cellular toxicity or any cellular morphology changes. To overcome the low cell
6 membrane permeability of SGM,³⁸ we performed cell electroporation in the presence of three
7 different concentration of SGM (0.01 mM, 0.1 mM, and 1 mM). Electroporation was carried out
8 along with a pmaxGFP plasmid to allow fluorescence microscopy observation and possibly detect
9 any morphological changes. Cells were observed after an overnight incubation. The number of
10 cells in the sample electroporated with SGM was comparable to the control (electroporation only
11 with pmaxGFP plasmid) (Supplementary Figure 14a), even at the highest SGM concentration,
12 which indicates that the concentrations of SGM that were used do not affect cell survival. No
13 microscopic effects on cell morphology could be detected for HepG2 (Figure 5d; Supplementary
14 Figure 14b and c) nor any change in the cell survival. The same experiment was performed using
15 different concentration of SAM (0.01 mM, 0.1 mM, and 1 mM), for HepG2 (Figure 5d;
16 Supplementary Figure 14d and e) resulting in the same observations. Since SGM carries the same
17 methyl transferring group as SAM, it is possible that SGM can neutrally substitute for SAM in the
18 methylation or polyamine downstream pathways (Supplementary Figure 15), or that it is simply
19 inert. Overall, we have shown that hMAT2A produces SGM *in vivo*, that SGM (and/or its
20 breakdown product MTG) is present in the cancer cell line HepG2 in which hMAT2A is
21 upregulated, suggesting that it could be potentially used as a biomarker, and that SGM is not toxic
22 for human cells within the parameters of this experiment.

23

24 **Discussion**

25

26 The enzyme kinetics and structural analysis suggests that the catalytic specificity of eMAT is a
27 result of the non-cognate ligands failing to adopt catalytically competent binding modes, whereas
28 in hMAT2A non-cognate substrates appear to be stabilized comparably to ATP. This leads to two
29 questions: first, why are the unique substrate binding modes observed in the eMAT:UTP
30 simulations not catalytically competent? The sulfur of methionine performs its nucleophilic
31 substitution at the ribose C5' atom; thus, the accessibility of this atom is of paramount importance.

1 In the non-productive states sampled by UTP throughout the simulation, the position of the C5'
2 atom is sterically occluded by the pyrimidine ring and methionine binding is sterically blocked
3 (Supplementary Figure 11). Clearly, UTP is a viable substrate for eMAT; indeed, we observe in
4 the MD simulations that catalytically productive enzyme: substrate complexes are stable for tens
5 of ns. Thus, the disorder observed here is best conceptualized as a partial depletion of catalytically
6 productive substrate binding, compared with the cognate substrate, ATP. The second question is:
7 why are the structural dynamics of the active site loop different between hMAT2A and eMAT?
8 The active sites are essentially identical (20/21 residues) and substitutions of Ser/Thr in either
9 enzyme at the one variant position has no effect on specificity. Thus, the structural explanation
10 must be found outside the active site. There are many sequence differences between eMAT and
11 hMAT2A in the second-third shell of the active site loop (Supplementary Figure 16). A plausible
12 explanation is therefore that additional stabilizing interactions in the closed state in hMAT2A mean
13 that it can remain closed with non-cognate substrates, even though the substrates provide fewer
14 stabilizing interactions. In contrast, eMAT cannot as easily sustain the closed active site loop
15 conformation without the additional stabilizing interactions from the adenine group, which are not
16 present in the binding modes of the other non-cognate nucleotides.

17
18 The selective pressure that drove the divergence in catalytic specificity between these orthologous
19 enzymes most likely relates to the different cellular abundance of these molecules, i.e., there has
20 been little selective pressure for hMAT2A to be specific because the other NTPs are not present at
21 sufficiently high concentrations to compete with ATP. Indeed, the concentration of ATP is ~10-
22 fold higher than the K_M , whereas for GTP/CTP/UTP the physiological concentrations are at or
23 below the respective K_M values (Table 1). In contrast, the concentrations of these NTPs in *E. coli*
24 are more similar: ATP is 3.5 mM while GTP is 1.6 mM. Thus, eMAT likely evolved specificity
25 owing to the selective pressure to discriminate between ATP and other nucleotides: the K_M of
26 eMAT for ATP is at least 16-fold lower than for any of the non-cognate NTPs (Table 1).

27
28 Finally, in this work we showed how MAT promiscuity is relevant *in vivo* as putative example of
29 “underground metabolism”¹⁰. It is thought that promiscuous functions of enzymes are likely to be
30 physiologically irrelevant¹. For instance, many promiscuous activities cannot occur at sufficiently
31 high frequency to be relevant owing to the substrate concentrations encountered in physiological

1 contexts³⁹, or the extremely low catalytic efficiency of many promiscuous activities making it
2 irrelevant on biological timescales⁴⁰⁻⁴². This study is therefore a rare example where we could
3 detect the promiscuous activity of hMAT2A for GTP *in vivo*. Moreover, we showed that it could
4 be used as a biomarker to distinguish between normal and cancer cell lines.

5
6 In summary, these results show how enzyme dynamics have substantial effects on the
7 conformational sampling of substrates within the active site of an enzyme, which can in turn result
8 in large changes in catalytic specificity. The concept of non-productive substrate binding is not
9 new⁴³, nor is the notion that protein dynamics can affect substrate turnover^{44,45}, but this is an
10 interesting example where the link between these two effects can be clearly seen. Moreover,
11 because we have compared orthologous enzymes that have been on different evolutionary
12 trajectories because of their distinct cellular environments, we have been able to show that the
13 sequence differences controlling this specificity originate in the outer shells of the active site,
14 which builds on a growing body of work that supports a model in which these outer-shell residues
15 are critical for maintaining the optimum active site architecture and controlling conformational
16 changes that are important in the catalytic cycle¹⁵. Consideration of these effects should aid
17 enzyme engineers, evolutionists and synthetic chemists in the design and study of enzymes,
18 substrates and inhibitors. For example, we hope that this work will aid in the design of SAM
19 analogues with unnatural bases; such analogues could show promise for reaching cellular bio-
20 orthogonal probes or inhibitors of methyltransferases.

21

22 **Methods**

23

24 **Protein expression and purification.** The eMAT plasmid was a generous gift from Prof. Ronald
25 E. Viola. *E. coli* BL21 (DE3) cells were transformed with the eMAT plasmid and protein was
26 expressed as reported previously¹⁹. Cell pellets were resuspended in Lysis Buffer (40 mM Tris-
27 HCl pH 8.0, 300 mM NaCl, 10 mM Imidazole) supplemented with 0.5 units turbonuclease (T4330,
28 Sigma Aldrich), 0.3 mg.ml⁻¹ lysozyme, 0.2 mM PMSF and 5 mM DTT. Solubilised pellets were
29 lysed by sonication and centrifuged at 30,000 × g for 30 min. The soluble fraction was applied to
30 a 5 mL HisTrap HP Ni²⁺-NTA IMAC column (GE Healthcare) pre-equilibrated with lysis buffer

1 and washed with 50 mM Imidazole. eMAT was eluted in lysis buffer supplemented with 400 mM
2 imidazole and concentrated with an Amicon Ultra-15 spin concentrator (30 kDa MW cutoff,
3 Milipore). eMAT was further purified by size exclusion chromatography (SEC) using a HiLoad®
4 26/600 Superdex 200 pg column (GE Healthcare) in SEC Buffer A (50 mM Tris-HCl pH 8.0,
5 100 mM NaCl and 5 mM DTT). Analysis of MAT protein purity was verified with Coomassie
6 SDS polyacrylamide gel electrophoresis and protein concentrations were calculated using the
7 molar extinction coefficient predicted by the ExPASy ProtParam server tool at A_{280} . The hMAT2A
8 plasmid was gift from the Jon S. Thorson and purified as reported⁴⁶. hMAT2A pellets were
9 processed in the same manner as eMAT, using sonication and Ni^{2+} -NTA IMAC except for the
10 composition of lysis buffer (50 mM Na_2HPO_4 pH 8.0, 300 mM NaCl and 10 mM imidazole).
11 hMAT2A elution was then incubated with 10 mM L-methionine, 10 mM $MgCl_2$ and 100 μ M
12 UppNHp for 1h on ice before purification in SEC Buffer B (25 mM HEPES pH 7.6, 150 mM
13 NaCl, 5 mM KCl, 5 mM DTT and 10% (v/v) glycerol).

14
15 **Protein crystallization, data collection and structure determination.** eMAT crystals were
16 grown at 19 °C using the hanging-drop vapour diffusion method with reservoir solutions
17 containing 0.1 M BIS-TRIS pH 6.5 and 10-20% (v/v) ethylene glycol while screening two different
18 lengths of polyethylene glycol (PEG) at varying concentrations: PEG 8000 from 6-9 % (w/v) and
19 PEG 3350 from 16-22 % (w/v). Drops were setup at 1:1 ratio and 1:2 ratio of reservoir to protein
20 volume. Co-crystals formed within 2-4 days at 19 °C with various substrates. hMAT2A-UppNHp
21 was concentrated to 10 mg.ml⁻¹ for protein X-ray crystallographic studies. hMAT2A-UppNHp
22 hanging drops were grown at 19 °C at a 1:1 and 1:2 ratio of reservoir to protein volume. The
23 optimised screening matrix consist of 0.1 M BIS-TRIS pH 6.5 and 10% (v/v) ethylene glycol while
24 screening PEG 3350 at concentrations of 7-10% (w/v). Cubic diamond crystals formed within 2
25 days at 19 °C. The co-crystals were cryoprotected in solutions containing the mother liquor and
26 increasing the concentrations of PEG 8000 or PEG 3350 to 25-35% (w/v) before being flash-
27 frozen in liquid nitrogen. Diffraction data was collected on the macromolecular crystallography
28 beamline (MX2) at the Australian Synchrotron using the Eiger X 6M detector at a wavelength of
29 0.9537 Å⁴⁷. Data was processed using XDS⁴⁸ and Aimless⁴⁹, and molecular replacement was
30 performed using Phaser⁵⁰. Iterative cycles of manual model building and refinement were
31 performed using Coot 0.9.3⁵¹ and phenix.refine⁵². Iterative cycles of manual model building and

1 refinement were performed using Coot 0.9.3⁵¹, and phenix.refine⁵². TLS refinement was used in
2 all cases, using TLS groups automatically selected by phenix.refine. Notably, chain B in the
3 hexagonal space groups exhibited significant disorder in places. All crystallization conditions, data
4 collection and refinement details are provided in Supplementary Table 1.

5

6 **Molecular dynamics simulations**

7

8 All molecular dynamics simulations were carried out using GROMACS 2018.4⁵³ with the eMAT-
9 ATP crystal structure as the starting point. For eMAT-UTP simulations, UTP was modelled in the
10 eMAT-ATP crystal structure at the ATP position. Chain termini were capped with neutral acetyl
11 and methylamide groups. Completed structures were solvated in a dodecahedral simulation box
12 with a minimum distance of 10 Å from any protein atom to the box wall, followed by addition of
13 roughly 50mM KCl into the aqueous phase, neutralizing the system charge. All systems were
14 subjected to steepest-descent energy minimisation followed by a 100 ps equilibration in the NVT
15 ensemble with position restraints of 1000 kJ/mol/nm² on all protein atoms, with velocities
16 initialising from a Maxwell distribution at 300 K. For NVT equilibration, 3 replicate equilibration
17 trajectories were independently initialised from energy minimised systems of each condition (i.e.
18 eMAT-ATP and eMAT-UTP), for a total of 6 NVT equilibration trajectories. All NVT-
19 equilibrated systems were then subjected to 100 ps equilibration in the NPT ensemble with position
20 restraints of 1000 kJ/mol/nm² on all protein atoms. Position restraints were released, and free
21 simulation performed at 300 K for 250 ns for each replicate. All simulations were performed using
22 the CHARMM36-mar2019 forcefield⁵⁴. Water explicitly modelled using the single-point charge
23 SPC216 model⁵⁵. Ionisable residues were set to their standard protonation state at pH 7. All
24 equilibration and production simulations were conducted under periodic boundary conditions.
25 Temperature was maintained close to the reference value of 300 K using V-rescale temperature
26 coupling. Pressure was maintained close to the reference value of 1 atm in NPT equilibration by
27 isotropic coupling with a Berendsen pressure bath; in production simulations, the Parinello-
28 Rahman barostat with isotropic pressure coupling was used. The LINCS algorithm⁵⁶ was used to
29 constrain the lengths of all bonds to hydrogen. The Verlet cut-off scheme was used to evaluate the
30 non-bonded interaction pair lists. Van der Waals interactions were evaluated using a simple cut-
31 off scheme with a radius of 12 Å. Coulomb interactions were evaluated using the Particle Mesh

1 Ewald (PME) method, with a real-space cut-off at 12 Å. A 2-fs time-step was used for integrating
2 the equations of motion. GROMACS tools⁵³ were used for correction of periodic boundary
3 conditions, RMSD and RMSF calculations. Graphs were prepared using custom scripts. Visual
4 Molecular Dynamics (VMD)⁵⁷ and PyMOL (The PyMOL Molecular Graphics System, Version
5 2.0 Schrödinger, LLC.) were used to view trajectories and prepare figures.

6 7 **Mutagenesis**

8 Site directed mutagenesis for S269T mutation on hMAT2A plasmid and T227S mutation on eMAT
9 plasmid was carried out using Q5 Site-Directed Mutagenesis Kit (NEB) by following kit protocol
10 and expressed, purified as hMAT2A and eMAT, respectively. The primers used for mutagenesis
11 listed in Supplementary table 3.

12 13 **Kinetics Assay for MATs**

14 To observe the reaction efficiency of SNM product formation during catalysis with different
15 substrates, purified eMAT at 5 mg.ml⁻¹ was incubated with 10 mM L-methionine, 10 mM MgCl₂
16 and different substrates at 100 μM (NTPs) respectively for 1h on ice. ATP/GTP/CTP/UTP (5 mM),
17 methionine (10 mM), HEPES (100 mM), MgCl₂ (10 mM), KCl (50 mM) and
18 hMAT2A/eMAT/S269T hMAT2A (20 μM) were mixed in water, pH was adjusted to 8 with 10%
19 NaOH. The reactions were incubated at 37 °C for 1 hr. Reaction was quench by acetonitrile
20 followed by centrifugation at 12,000 RPM for 5 min to precipitate the enzymes. Finally,
21 supernatant was filtered through 0.22 μm filter (Merck) and injected in UPLC for analysis (Waters
22 UPLC Acquity H class). Diluted reaction aliquots were analyzed by using a HILIC column
23 (SeQuant ZIC-chILIC 3 μm, 100 Å 150 x 2.1 mm PEEK coated HPLC column). An isocratic
24 method was used with solvent A (100 mM ammonium acetate, pH 5.3) 35% and solvent B
25 (acetonitrile) 65% for 15 min. Each injection was 3 μL with a flow rate of 0.3 mL/min and detected
26 at 260 nm. Using this UPLC method retention times for molecules were MTA 1.3 min, MTU 1.3
27 min, MTC 1.4 min, MTG 1.5 min, adenine 1.6 min, uracil 1.6 min, cytosine 1.8 min, guanine 2
28 min, SAM 4.1 min, SCM 4.6 min, SUM 4.6 min, SGM 5.3 min, ADP 5.3 min, UDP 6 min, CDP
29 6.1 min, GDP 6.3 min, ATP 7.5 min, GTP 7.8 min, CTP 8.3 min. Product formation was further
30 confirmed by mass analysis (Appendix). SNM were purified using above mentioned UPLC
31 method and standard curves were plotted. For kinetic assay concentrations of the NTPs were in

1 the range of 0.0251-5 mM and constant methionine concentration 10 mM were used. The kinetic
2 parameters were determined using the Michaels-Menten equation using GraphPad Prism. The
3 release of nucleotide bases from SNM analogs were also detected by UPLC (Supplementary Figure
4 5A). SAM is prone to alkaline depurination⁵⁸ but release of nucleotide bases for pyrimidine ring
5 in our reaction conditions might be due to deprotonation at C-5' in basic conditions followed by
6 the opening of the ribose ring which eliminates nucleotide base, further attack of water reforms
7 ribose ring to give S-ribosylmethionine⁵⁹. Elimination of nucleotide bases was not observed from
8 NTPs (Supplementary Figure 2B) under the same conditions, which demonstrate that release of
9 nucleotide base was from SNM analogs.

10

11 **Analytical Size Exclusion chromatography**

12 Size exclusion chromatography was performed using GE Healthcare Life Sciences using Superdex
13 200 Increase 10/300 GL column. Injection volume was 100 μ L, detection at 280 nm and flow rate
14 was 0.3 mL/min. Nonhydrolyzable NTPs (1 mM) Adenosine-5'-[(β , γ)-imido]triphosphate
15 (AppNHp), Guanosine-5'-[(β , γ)-imido]triphosphate (GppNHp), Cytidine-5'-[(β , γ)-methyleno]
16 triphosphate (CppCp), Uridine-5'-[(β , γ)-imido]triphosphate (UppNHp)] were incubated with
17 methionine (L-Met) (10 mM) in HEPES (100 mM), KCl (50 mM), MgCl₂ (10 mM), pH 8 at 37 °C
18 for 1 hr and then injected in the column.

19

20 **Cell culture and extraction of metabolites**

21 HepG2 was grown in DMEM medium containing 10% FBS and penicillin (100 U/ml),
22 streptomycin (100 mg/ml) by incubation in a 5% CO₂ at 37 °C with 95% humidity. For routine
23 maintenance, cells were trypsinized and split before becoming fully confluent. Cultured cells were
24 washed with cold PBS (5 mL) twice. Cells (20 M) were harvested by trypsinization using TrypLE
25 Express Enzyme (1X), no phenol red for 3 min at 37 °C in CO₂ incubator. Centrifuged for 5 min
26 at 100g. TrypLE was discarded and pellet was resuspended into cold PBS. Cell pellet was washed
27 with cold PBS twice. Further extraction steps were performed on ice. Internal standards (10 nmol
28 of HEPES and PIPES) were added to sample. Cells were disrupted using 1 mL of cold acetonitrile,
29 methanol, water (40:40:20) with 0.1 M formic acid and glass beads acid washed, by vortexing.
30 Metabolites were collected by the centrifugation. Samples were concentrated using speed vac and

1 finally dissolved in 100 μ L of 10% acetonitrile with 0.1% formic acid and filtered through a 0.22
2 μ m filter and injected into LC-MS.

3 **LC-MS method for metabolite analysis**

4 Data were collected using Q-Exactive HF mass spectrometer (Thermo Fisher Scientific) coupled
5 with Waters UPLC ACQUITY M-Class liquid chromatography system. An analytical column
6 (ACQUITY UPLC HSS T3 1.8 μ m, 1.0 x 150 mm) was used for sample chromatographic
7 separation. An injection volume of 2 μ L was separated at flow rate of 50 μ L/min using a gradient
8 of 10–95% solvent B over 8 min, using water with 0.1% formic acid as solvent A and acetonitrile
9 with 0.1% formic acid as solvent B. MS data were collected using Q-Exactive HF mass
10 spectrometer (Thermo Fisher Scientific). The parameters are listed here: spray voltage, 3.0 kV;
11 sheath gas, 16; auxiliary gas, 2; capillary temperature, 250 $^{\circ}$ C; aux gas heater temp, 150 $^{\circ}$ C; S-lens
12 RF, 50; tuning method name, HESI; Spray interface, HESI, with metal needle for small flow (1 to
13 10 μ L/min). The mass spectrometry method was set to acquire MS1 data for 14 min, positive
14 mode, mass range 80 to 1,000 m/z. Resolution was set at 60,000. Maximum injection time was 30
15 ms. Auto gain was targeted to 500000 ions. Extracted ion chromatograms were done using a 5-
16 ppm tolerance and smoothing with Boxcar method using 7 points.

17

18 **Cell electroporation with SGM, SAM and pmaxGFP Plasmid**

19 Cells were harvested by trypsinization and 2×10^6 cells were pelleted by centrifugation at 100g for
20 3 min. Cells were resuspended in Nucleofector solution from Lonza. SF cell line 4d-Nucleofactor
21 X kit S (V4XC-2032) for HepG2 cells. Cells were electroporated with 0.4 μ g pmaxGFP plasmid
22 and different concentrations of SGM and SAM (0.01, 0.1, 1 mM) using 4D-Nucleofactor X Unit
23 from Lonza. EH-100 program was used for HepG2 by following the manufactures protocol. Cells
24 were incubated overnight in the incubator and observed under the fluorescence microscope. Cells
25 were observed using Leica DMiL microscope using 10X objective. For higher magnification cells
26 were observed using ZEISS Celldiscoverer 7 using 20X objective with 2 \times magnification changer.

27

28 **Author contributions**

29 M.G. performed MAT kinetics assay (including protein purification), ran SEC analysis, performed
30 all the cell experiments (including culturing), metabolites extractions, imaging, processed and
31 analyzed data. M.G., A.V.B ran LC-MS for metabolites, processed and analyzed data.

1 L.L.T. expressed and purified protein for crystallography and collected crystallographic data.
2 L.L.T., A.D., J.S.B. C.J.J. processed, solved, and analyzed crystallographic data. M.S. performed
3 molecular dynamics simulations. P.L. and C. J. J. analyzed data and wrote the paper with inputs
4 of M.G. P. L., and C.J.J. supervised the project.

6 **Acknowledgments**

7 We thank Yohsuke Moriyama for assistance with the cell electroporation experiment and Keiko
8 Kono to share the fluorescent microscope in her Unit. We thank Saacnicteh Toledo-Patino and
9 Benjamin Clifton for insightful comments on this manuscript.

10

11 **Funding**

12 Financial support by the Okinawa Institute of Science and Technology to P.L. is gratefully
13 acknowledged. Laurino lab is supported by Kakenhi Grant (# 90812256). This project was
14 supported by OIST Kick start up grant. Funding by the Australian Research Council for the Centres
15 of Excellence in Synthetic Biology and Innovation in Peptide and Protein Science is gratefully
16 acknowledged. This research was undertaken in part using the MX2 beamline at the Australian
17 Synchrotron, part of ANSTO, and made use of the Australian Cancer Research Foundation
18 (ACRF) detector.

19

20

21

22 **References**

- 23 1. Copley, S.D. Shining a light on enzyme promiscuity. *Curr Opin Struct Biol* **47**, 167-175 (2017).
- 24 2. O'Brien, P.J. & Herschlag, D. Catalytic promiscuity and the evolution of new enzymatic activities.
25 *Chem Biol* **6**, R91-R105 (1999).
- 26 3. Jensen, R.A. Enzyme recruitment in evolution of new function. *Annu Rev Microbiol* **30**, 409-25
27 (1976).
- 28 4. Khersonsky, O., Roodveldt, C. & Tawfik, D.S. Enzyme promiscuity: evolutionary and mechanistic
29 aspects. *Curr Opin Chem Biol* **10**, 498-508 (2006).
- 30 5. Copley, S.D. Enzymes with extra talents: moonlighting functions and catalytic promiscuity. *Curr*
31 *Opin Chem Biol* **7**, 265-72 (2003).
- 32 6. Jeffery, C.J. Moonlighting proteins. *Trends Biochem Sci* **24**, 8-11 (1999).
- 33 7. Khersonsky, O. & Tawfik, D.S. Enzyme promiscuity: a mechanistic and evolutionary perspective.
34 *Annu Rev Biochem* **79**, 471-505 (2010).

- 1 8. Piedrafita, G., Keller, M.A. & Ralser, M. The Impact of Non-Enzymatic Reactions and Enzyme
2 Promiscuity on Cellular Metabolism during (Oxidative) Stress Conditions. *Biomolecules* **5**, 2101-
3 22 (2015).
- 4 9. Ward, P.S. et al. The common feature of leukemia-associated IDH1 and IDH2 mutations is a
5 neomorphic enzyme activity converting alpha-ketoglutarate to 2-hydroxyglutarate. *Cancer Cell* **17**,
6 225-34 (2010).
- 7 10. D'Ari, R. & Casadesus, J. Underground metabolism. *Bioessays* **20**, 181-6 (1998).
- 8 11. Gora, A., Brezovsky, J. & Damborsky, J. Gates of enzymes. *Chem Rev* **113**, 5871-923 (2013).
- 9 12. Tokuriki, N. & Tawfik, D.S. Protein dynamism and evolvability. *Science* **324**, 203-7 (2009).
- 10 13. Maria-Solano, M.A., Serrano-Hervas, E., Romero-Rivera, A., Iglesias-Fernandez, J. & Osuna, S.
11 Role of conformational dynamics in the evolution of novel enzyme function. *Chem Commun*
12 (*Camb*) **54**, 6622-6634 (2018).
- 13 14. Clifton, B.E. & Jackson, C.J. Ancestral Protein Reconstruction Yields Insights into Adaptive
14 Evolution of Binding Specificity in Solute-Binding Proteins. *Cell Chem Biol* **23**, 236-245 (2016).
- 15 15. Campbell, E. et al. The role of protein dynamics in the evolution of new enzyme function. *Nat*
16 *Chem Biol* **12**, 944-950 (2016).
- 17 16. Barrozo, A., Duarte, F., Bauer, P., Carvalho, A.T. & Kamerlin, S.C. Cooperative Electrostatic
18 Interactions Drive Functional Evolution in the Alkaline Phosphatase Superfamily. *J Am Chem Soc*
19 **137**, 9061-76 (2015).
- 20 17. Jones, B.J. et al. Larger active site in an ancestral hydroxynitrile lyase increases catalytically
21 promiscuous esterase activity. *PLoS One* **15**, e0235341 (2020).
- 22 18. Miton, C.M. et al. Evolutionary repurposing of a sulfatase: A new Michaelis complex leads to
23 efficient transition state charge offset. *Proc Natl Acad Sci U S A* **115**, E7293-E7302 (2018).
- 24 19. Parungao, G.G. et al. Complementation of a metK-deficient E. coli strain with heterologous
25 AdoMet synthetase genes. *Microbiology* **163**, 1812-1821 (2017).
- 26 20. Markham, G.D. & Pajares, M.A. Structure-function relationships in methionine
27 adenosyltransferases. *Cell Mol Life Sci* **66**, 636-48 (2009).
- 28 21. Merali, S. & Clarkson, A.B., Jr. S-adenosylmethionine and Pneumocystis. *FEMS Microbiol Lett*
29 **237**, 179-86 (2004).
- 30 22. Lu, S.C. & Mato, J.M. S-adenosylmethionine in liver health, injury, and cancer. *Physiol Rev* **92**,
31 1515-42 (2012).
- 32 23. Zhao, M., Wijayasinghe, Y.S., Bhansali, P., Viola, R.E. & Blumenthal, R.M. A surprising range of
33 modified-methionyl S-adenosylmethionine analogues support bacterial growth. *Microbiology* **161**,
34 674-82 (2015).
- 35 24. Cantoni, G.L. The Nature of the Active Methyl Donor Formed Enzymatically from L-Methionine
36 and Adenosinetriphosphate. *Journal of the American Chemical Society* **74**, 2942-2943 (1952).
- 37 25. Mudd, S.H. & Cantoni, G.L. Activation of methionine for transmethylatation. III. The methionine-
38 activating enzyme of Bakers' yeast. *J Biol Chem* **231**, 481-92 (1958).
- 39 26. McQueney, M.S., Anderson, K.S. & Markham, G.D. Energetics of S-adenosylmethionine
40 synthetase catalysis. *Biochemistry* **39**, 4443-54 (2000).
- 41 27. Lu, Z.J. & Markham, G.D. Enzymatic properties of S-adenosylmethionine synthetase from the
42 archaeon *Methanococcus jannaschii*. *J Biol Chem* **277**, 16624-31 (2002).
- 43 28. Komoto, J., Yamada, T., Takata, Y., Markham, G.D. & Takusagawa, F. Crystal structure of the S-
44 adenosylmethionine synthetase ternary complex: A novel catalytic mechanism of S-
45 adenosylmethionine synthesis from ATP and Met. *Biochemistry* **43**, 1821-1831 (2004).
- 46 29. Levy, M. & Miller, S.L. The stability of the RNA bases: implications for the origin of life. *Proc*
47 *Natl Acad Sci U S A* **95**, 7933-8 (1998).
- 48 30. Takusagawa, F., Kamitori, S., Misaki, S. & Markham, G.D. Crystal structure of S-
49 adenosylmethionine synthetase. *Journal of Biological Chemistry* **271**, 136-147 (1996).
- 50 31. Murray, B. et al. Crystallography captures catalytic steps in human methionine adenosyltransferase
51 enzymes. *Proc Natl Acad Sci U S A* **113**, 2104-9 (2016).

- 1 32. Markham, G.D., Hafner, E.W., Tabor, C.W. & Tabor, H. S-Adenosylmethionine synthetase from
2 Escherichia coli. *J Biol Chem* **255**, 9082-92 (1980).
- 3 33. Traut, T.W. Physiological concentrations of purines and pyrimidines. *Mol Cell Biochem* **140**, 1-22
4 (1994).
- 5 34. Buckstein, M.H., He, J. & Rubin, H. Characterization of nucleotide pools as a function of
6 physiological state in Escherichia coli. *J Bacteriol* **190**, 718-26 (2008).
- 7 35. Cai, J., Mao, Z., Hwang, J.J. & Lu, S.C. Differential expression of methionine adenosyltransferase
8 genes influences the rate of growth of human hepatocellular carcinoma cells. *Cancer Res* **58**, 1444-
9 50 (1998).
- 10 36. Chang, C.F., Liau, M.C. & Becker, F.F. Alteration of S-Adenosylmethionine Synthetases during
11 Chemical Hepatocarcinogenesis and in Resulting Carcinomas. *Proceedings of the American*
12 *Association for Cancer Research* **20**, 13-13 (1979).
- 13 37. Paneda, C. et al. Liver cell proliferation requires methionine adenosyltransferase 2A mRNA up-
14 regulation. *Hepatology* **35**, 1381-91 (2002).
- 15 38. Wang, R., Zheng, W. & Luo, M. A sensitive mass spectrum assay to characterize engineered
16 methionine adenosyltransferases with S-alkyl methionine analogues as substrates. *Anal Biochem*
17 **450**, 11-9 (2014).
- 18 39. Bar-Even, A., Milo, R., Noor, E. & Tawfik, D.S. The Moderately Efficient Enzyme: Futile
19 Encounters and Enzyme Floppiness. *Biochemistry* **54**, 4969-77 (2015).
- 20 40. Copley, S.D. An evolutionary biochemist's perspective on promiscuity. *Trends Biochem Sci* **40**, 72-
21 8 (2015).
- 22 41. McLoughlin, S.Y. & Copley, S.D. A compromise required by gene sharing enables survival:
23 Implications for evolution of new enzyme activities. *Proc Natl Acad Sci U S A* **105**, 13497-502
24 (2008).
- 25 42. Khanal, A., Yu McLoughlin, S., Kershner, J.P. & Copley, S.D. Differential effects of a mutation
26 on the normal and promiscuous activities of orthologs: implications for natural and directed
27 evolution. *Mol Biol Evol* **32**, 100-8 (2015).
- 28 43. Natarajan, S.K. & Sierks, M.R. Minimizing nonproductive substrate binding: a new look at
29 glucoamylase subsite affinities. *Biochemistry* **36**, 14946-55 (1997).
- 30 44. Agarwal, P.K. Role of protein dynamics in reaction rate enhancement by enzymes. *J Am Chem Soc*
31 **127**, 15248-56 (2005).
- 32 45. Tousignant, A. & Pelletier, J.N. Protein motions promote catalysis. *Chem Biol* **11**, 1037-42 (2004).
- 33 46. Singh, S. et al. Facile chemoenzymatic strategies for the synthesis and utilization of S-adenosyl-
34 (L)-methionine analogues. *Angew Chem Int Ed Engl* **53**, 3965-9 (2014).
- 35 47. McPhillips, T.M. et al. Blu-Ice and the Distributed Control System: software for data acquisition
36 and instrument control at macromolecular crystallography beamlines. *J Synchrotron Radiat* **9**, 401-
37 6 (2002).
- 38 48. Kabsch, W. Xds. *Acta Crystallogr D Biol Crystallogr* **66**, 125-32 (2010).
- 39 49. Evans, P.R. & Murshudov, G.N. How good are my data and what is the resolution? *Acta*
40 *Crystallogr D Biol Crystallogr* **69**, 1204-14 (2013).
- 41 50. McCoy, A.J. et al. Phaser crystallographic software. *J Appl Crystallogr* **40**, 658-674 (2007).
- 42 51. Emsley, P., Lohkamp, B., Scott, W.G. & Cowtan, K. Features and development of Coot. *Acta*
43 *Crystallogr D Biol Crystallogr* **66**, 486-501 (2010).
- 44 52. Afonine, P.V. et al. Towards automated crystallographic structure refinement with phenix.refine.
45 *Acta Crystallogr D Biol Crystallogr* **68**, 352-67 (2012).
- 46 53. Abraham, M.J. et al. GROMACS: High performance molecular simulations through multi-level
47 parallelism from laptops to supercomputers. *SoftwareX* **1-2**, 19-25 (2015).
- 48 54. Huang, J. et al. CHARMM36m: an improved force field for folded and intrinsically disordered
49 proteins. *Nat Methods* **14**, 71-73 (2017).
- 50 55. Darden, T., York, D. & Pedersen, L. Particle mesh Ewald: An N·log(N) method for Ewald sums in
51 large systems. *The Journal of Chemical Physics* **98**, 10089-10092 (1993).

- 1 56. Hess, B., Bekker, H., Berendsen, H.J.C. & Fraaije, J.G.E.M. LINCS: A linear constraint solver for
2 molecular simulations. *Journal of Computational Chemistry* **18**, 1463-1472 (1997).
3 57. Humphrey, W., Dalke, A. & Schulten, K. VMD: visual molecular dynamics. *J Mol Graph* **14**, 33-
4 8, 27-8 (1996).
5 58. Parks, L.W. & Schlenk, F. The stability and hydrolysis of S-adenosylmethionine; isolation of S-
6 ribosylmethionine. *J Biol Chem* **230**, 295-305 (1958).
7 59. Iwig, D.F. & Booker, S.J. Insight into the polar reactivity of the onium chalcogen analogues of S-
8 adenosyl-L-methionine. *Biochemistry* **43**, 13496-509 (2004).
9